

ARTICLE OPEN



High-mobility two-dimensional carriers from surface Fermi arcs in magnetic Weyl semimetal films

Shingo Kaneta-Takada^{1,2,8}, Yuki K. Wakabayashi^{1,8}, Yoshiharu Krockenberger¹, Toshihiro Nomura³, Yoshimitsu Kohama³, Sergey A. Nikolaev^{4,5}, Hena Das^{4,5,6}, Hiroshi Irie¹, Kosuke Takiguchi^{1,2}, Shinobu Ohya^{1,2,7}, Masaaki Tanaka^{1,2,7}, Yoshitaka Taniyasu¹ and Hideki Yamamoto¹

High-mobility two-dimensional carriers originating from surface Fermi arcs in magnetic Weyl semimetals are highly desired for accessing exotic quantum transport phenomena and for topological electronics applications. Here, we demonstrate high-mobility two-dimensional carriers that show quantum oscillations in magnetic Weyl semimetal SrRuO₃ epitaxial films by systematic angle-dependent, high-magnetic field magnetotransport experiments. The exceptionally high-quality SrRuO₃ films were grown by state-of-the-art oxide thin film growth technologies driven by machine-learning algorithm. The quantum oscillations for the 10-nm SrRuO₃ film show a high quantum mobility of 3.5×10^3 cm²/Vs, a light cyclotron mass, and two-dimensional angular dependence, which possibly come from the surface Fermi arcs. The linear thickness dependence of the phase shift of the quantum oscillations provides evidence for the non-trivial nature of the quantum oscillations mediated by the surface Fermi arcs. In addition, at low temperatures and under magnetic fields of up to 52 T, the quantum limit of SrRuO₃ manifests the chiral anomaly of the Weyl nodes. Emergence of the hitherto hidden two-dimensional Weyl states in a ferromagnetic oxide paves the way to explore quantum transport phenomena for topological oxide electronics.

npj Quantum Materials (2022)7:102; <https://doi.org/10.1038/s41535-022-00511-0>

INTRODUCTION

High-mobility two-dimensional carriers were first realized at semiconductor surfaces and interfaces, where they form the basis of the integer and fractional quantum Hall effects^{1–4}, two-dimensional superconductivity⁵, and practical applications such as high-electron-mobility transistors^{6,7}. The two-dimensional carriers originating from the surface Fermi arcs or the quantum confinement of bulk three-dimensional Dirac fermions are reported for the Dirac semimetal Cd₃As₂^{8–15}. The high-mobility two-dimensional carriers are also pursued in Weyl semimetals and magnetic Weyl semimetals. Examples of Weyl semimetals and magnetic Weyl semimetals are TaAs^{16–19}, Na₃Bi^{20,21}, NbAs^{22,23}, Co₃Sn₂S₂^{24,25}, Co₂MnGa²⁶, and SrRuO₃²⁷. Since these states in topological semimetals are predicted to be robust against perturbations^{10,14,28,29}, they are of both scientific and technological interests, with potential for use in high-performance electronics, spintronics, and quantum computing. In particular, Weyl fermions in magnetic Weyl semimetals are thought to be more suitable for spintronic applications^{25,30,31}. Since the distribution of Weyl nodes in magnetic Weyl semimetals is determined by the spin texture^{27,32}, the high-mobility two-dimensional carriers originating from the Weyl nodes in magnetic Weyl semimetals are expected to be controllable by magnetization switching³³ in addition to the electric field^{6,13}. To detect these high-mobility two-dimensional carriers in transport measurements, high-quality epitaxial Weyl semimetal thin films, in which the contributions of surface states and/or quantum-confined bulk states are prominent, are needed. Conversely, the experimental detection

of these Weyl states in transport has remained elusive due to the lack of high-quality epitaxial Weyl semimetal films. Revealing the quantum transport properties of high-mobility two-dimensional carriers in magnetic Weyl semimetals is urgently required for a deep understanding of magnetic Weyl semimetals and demonstrating the relevance of Weyl fermions to spintronic and electronic applications.

The recent observation of the Weyl fermions in the itinerant 4d ferromagnetic perovskite SrRuO₃^{27,32,34}, which is widely used as an epitaxial conducting layer in oxide heterostructures^{35–46}, points to this material being an appropriate platform to integrate two emerging fields: topology in condensed matter and oxide electronics. Since the quantum transport of Weyl fermions in SrRuO₃ has been reported in high-quality epitaxial films²⁷, SrRuO₃ provides a promising opportunity to realize high-mobility two-dimensional carriers in magnetic Weyl semimetals. However, their dimensional character remains unsolved due to the lack of angle-dependent quantum oscillations. Since the amplitude of the quantum oscillation becomes small for angles close to the in-plane direction of the film, high-magnetic field transport measurements are indispensable to scrutinize the angular dependence of the quantum oscillations. Furthermore, high-magnetic field transport measurements will simultaneously provide information regarding the chiral anomaly in the quantum limit of Weyl fermions in SrRuO₃.

In this article, we present a systematic study of the angle-dependent magnetotransport, including quantum oscillations, up to 52 T in ultrahigh-quality SrRuO₃ thin films with thicknesses of

¹NTT Basic Research Laboratories, NTT Corporation, Atsugi, Kanagawa 243-0198, Japan. ²Department of Electrical Engineering and Information Systems, The University of Tokyo, Bunkyo, Tokyo 113-8656, Japan. ³Institute for Solid State Physics, The University of Tokyo, Kashiwa, Chiba 277-8581, Japan. ⁴Laboratory for Materials and Structures, Tokyo Institute of Technology, Yokohama, Kanagawa 226-8503, Japan. ⁵Tokyo Tech World Research Hub Initiative (WRHI), Institute of Innovative Research, Tokyo Institute of Technology, Yokohama, Kanagawa 226-8503, Japan. ⁶Kanagawa Institute of Industrial Science and Technology, 705-1 Shimoaizumi, Ebina-shi, Kanagawa 243-0435, Japan. ⁷Center for Spintronics Research Network (CSRN), The University of Tokyo, Bunkyo, Tokyo 113-8656, Japan. ⁸These authors contributed equally: Shingo Kaneta-Takada, Yuki K. Wakabayashi. ✉email: yuuki.wakabayashi.we@hco.ntt.co.jp

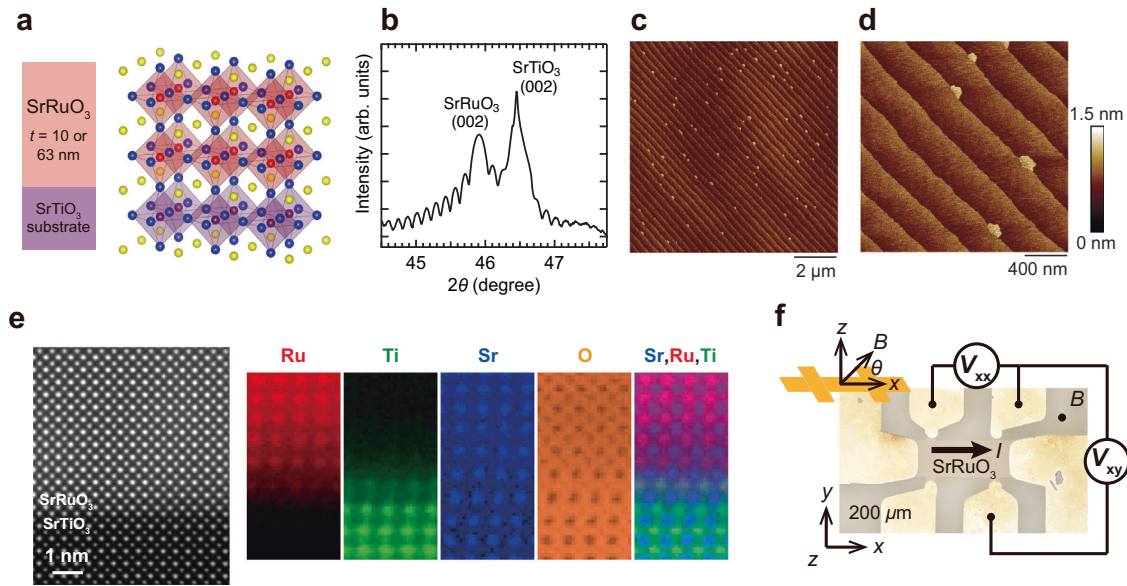


Fig. 1 Sample characteristics and Hall bar device of SrRuO₃. **a** Schematic of the sample and crystal structures of the SrRuO₃ films on a SrTiO₃ substrate¹⁰⁵. In the schematic crystal image, yellow, blue, red, and purple spheres indicate strontium, oxygen, ruthenium, and titanium, respectively. **b** XRD θ - 2θ scan of the SrRuO₃ film with $t = 63$ nm. **c** AFM image of the SrRuO₃ film with $t = 63$ nm. **d** Magnified image of **c**. **e** Cross-sectional high-angle annular dark field scanning transmission electron microscopy (HAADF-STEM) image of the SrRuO₃ film with $t = 63$ nm along the [100] axis of the SrTiO₃ substrate. EELS-STEM images (from left to right) for the Ru- $M_{4,5}$ - (red), Ti- $L_{2,3}$ - (green), Sr- M_{3} - (blue), O-K-edge (orange), and a color overlay of the EELS-STEM images for Sr, Ru, and Ti. **f** Optical microscope image of a Hall bar device. The current flows along the x direction, and the longitudinal and Hall voltage were measured using the V_{xx} and V_{xy} terminals. The upper left inset shows the arrangement of the Hall bar device and the magnetic field B .

10, 20, 40, 60, and 63 nm grown by machine-learning-assisted molecular beam epitaxy (MBE)^{47,48}. The quantum oscillations in resistivity [i.e., Shubnikov-de Haas (SdH) oscillations] for the 10-nm film show the light cyclotron mass of $0.25m_0$ (m_0 : free electron mass in a vacuum), high quantum mobility of 3.5×10^3 cm²/Vs, and two-dimensional angular dependence, confirming the existence of high-mobility two-dimensional carriers in SrRuO₃. The quantum oscillations for the 63-nm film, whose thickness is larger than the Fermi wavelength of the high-mobility carriers (~ 22.4 nm), also show the two-dimensional angular dependence, suggesting that the high-mobility two-dimensional carriers possibly come from the surface Fermi arcs, not the quantum confinement effect. The thickness-dependent phase shift establishes the non-trivial character of the quantum oscillations mediated from the surface Fermi arcs: The phase shift of the quantum oscillations shows a linear thickness dependence. We also observed the saturation of the chiral-anomaly-induced negative MR in the quantum limit, which had never been observed in magnetic Weyl semimetals. These findings of the high-mobility two-dimensional carriers and chiral anomaly in the quantum limit in an epitaxial ferromagnetic oxide provide an intriguing platform for topological oxide electronics and will stimulate further investigation of exotic quantum transport phenomena in epitaxial heterostructures.

RESULTS AND DISCUSSION

High-quality SrRuO₃ thin films

We grew high-quality epitaxial SrRuO₃ films with thicknesses $t = 10, 20, 40, 60,$ and 63 nm on (001) SrTiO₃ substrates (Fig. 1a) in a custom-designed molecular beam epitaxy (MBE) (see Methods section “Sample preparation” for details). The growth parameters, such as the growth temperature, supplied Ru/Sr flux ratio, and oxidation strength, were optimized by Bayesian optimization, a machine-learning technique for parameter optimization^{47,49,50}, with which we achieved a high residual resistivity ratio (RRR) of

19.2 and 81.0 with $t = 10$ and 63 nm, respectively. The high crystalline quality and large coherent volume of the epitaxial single-crystalline films were confirmed by θ - 2θ x-ray diffraction (XRD) and atomic force microscopy (AFM) (Fig. 1b–d; see Methods section “Sample preparation” for details). Epitaxial growth of the high-quality single-crystalline SrRuO₃ film with an abrupt substrate/film interface is seen in the electron energy loss spectroscopy-cross sectional scanning transmission microscopy (EELS-STEM) images (Fig. 1e).

Thickness-dependent magnetotransport

We performed magnetotransport measurements on the Hall bar devices of the SrRuO₃ film (Fig. 1f) with $t = 10$ nm using the PPMS (see Methods section “Magnetotransport measurements” for details). In Fig. 2, the ρ_{xx} , MR ($(\rho_{xx}(B) - \rho_{xx}(0\text{ T}))/\rho_{xx}(0\text{ T})$), and ρ_{xy} data for the SrRuO₃ film with $t = 63$ nm reported in ref. ²⁷, are also shown for comparison. The temperature T dependence of the longitudinal resistivity ρ_{xx} of the SrRuO₃ films is shown in Fig. 2a. The ρ_{xx} of the films with $t = 10$ and 63 nm decreased with decreasing temperature, indicating that these films are metallic over the whole temperature range. The temperature dependence of the normalized resistivity for the SrRuO₃ film with $t = 10$ nm is identical to that for the SrRuO₃ film with $t = 63$ nm. This result indicates that bulk electronic conduction in electrical transport is dominant even in the 10-nm thick film (see the Sec. I of the supplementary information). The ρ_{xx} vs. T curves show clear kinks (arrows in Fig. 2a), at which the ferromagnetic transition occurs, and spin-dependent scattering is suppressed⁴¹. The magnetization measurement for the SrRuO₃ film with $t = 63$ nm at $T = 10$ K shows a typical ferromagnetic hysteresis loop (left inset in Fig. 2a). As shown in the right inset in Fig. 2a, below 20 K, the SrRuO₃ films showed a T^2 scattering rate ($\rho \propto T^2$) that is expected for a Fermi liquid, in which electron-electron scattering dominates the transport and carriers are described as Landau quasiparticles^{27,41,51,52}. Although the RRR decreases from 81.0 to 19.2 with decreasing t from 63 to 10 nm, the RRR of the 10-nm film is high

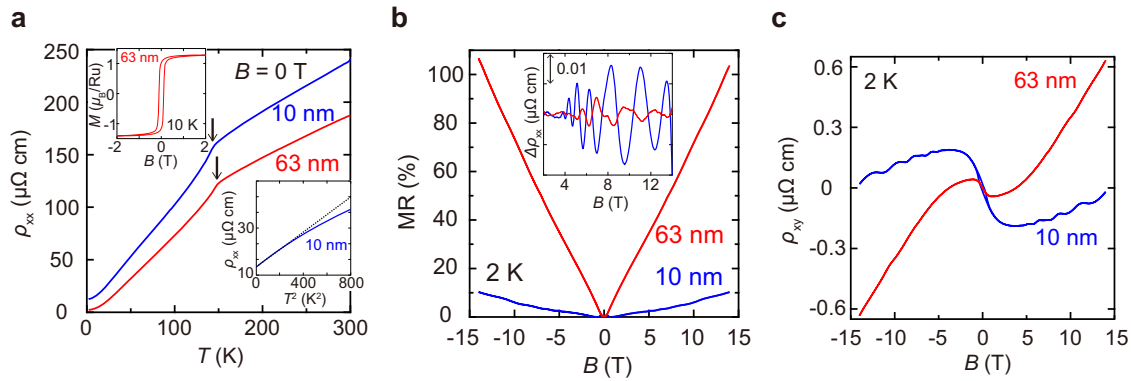


Fig. 2 Thickness dependence of the transport properties. **a** Temperature dependence of longitudinal resistivity ρ_{xx} for the SrRuO₃ films with $t = 10$ and 63 nm at zero magnetic field. The arrows indicate the ferromagnetic transition temperatures. The left inset shows the magnetization vs. magnetic field curve for the SrRuO₃ film with $t = 63$ nm at 10 K with B applied in the out-of-plane [001] direction of the SrTiO₃ substrate. The right inset shows the ρ_{xx} vs. T^2 plot with the linear fitting (black dashed line). **b** Thickness t dependence of MR ($(\rho_{xx}(B) - \rho_{xx}(0T))/\rho_{xx}(0T)$) at 2 K with B applied in the out-of-plane [001] direction of the SrTiO₃ substrate ($\theta = 90^\circ$). The inset shows the oscillation components obtained by subtracting a polynomial function up to the eighth order. **c** Thickness t dependence of transverse resistivity ρ_{xy} at 2 K with B applied in the out-of-plane [001] direction of the SrTiO₃ substrate ($\theta = 90^\circ$). Here, the ρ_{xx} , MR, and ρ_{xy} data for the SrRuO₃ film with $t = 63$ nm are the same data reported in ref. 27.

enough to observe the intrinsic quantum transport of Weyl fermions in SrRuO₃^{27,53}. The availability of such high-quality thin films allows obtaining insights into the dimensionality of the Weyl fermions in SrRuO₃ via measurements of angle-dependent magnetotransport properties, as will be described in the “High-mobility two-dimensional carriers” section. The larger residual resistivity ρ_{Res} at 2 K for the SrRuO₃ film with $t = 10$ nm suggests a disorder near the interface between SrRuO₃ and the SrTiO₃ substrate⁵³. Figure 2b shows the MR ($(\rho_{xx}(B) - \rho_{xx}(0T))/\rho_{xx}(0T)$) for the SrRuO₃ films with a magnetic field B applied in the out-of-plane [001] direction of the SrTiO₃ substrate at 2 K. Importantly, the linear positive MR at 2 K showed no signature of saturation even up to 14 T, which is commonly seen in Weyl semimetals^{9,19,54–57} and is thought to stem from the linear energy dispersion of Weyl nodes^{58–60}. In the Fermi liquid temperature range ($T < 20$ K), quantum lifetimes long enough to observe quantum oscillations were achieved, as evidenced by the observation of the SdH oscillations in both MR and ρ_{xy} (Fig. 2b, c). The SdH oscillations with the frequency $F \sim 25$ T for the thin film ($t = 10$ nm) is more prominent than that for the thick film ($t = 63$ nm), implying that the quantum oscillation has the surface origin. This is consistent with the fact that quantum oscillations with the frequency $F \sim 25$ T have only been observed in thin films^{27,51,53} and not in bulk samples⁵¹. As will be described in the “High-mobility two-dimensional carriers” section, the main component of the SdH oscillations for both films have the frequency $F \sim 25$ T, which was interpreted to be of the three-dimensional Weyl fermions with high mobility and light cyclotron mass in our previous study²⁷. For clarifying the dimensionality of the SdH oscillations, we investigated the angular dependence of the magnetotransport properties in the SrRuO₃ films. The angle-dependent magnetotransport measurements also provide experimental evidence of the chiral anomaly that Weyl fermions in SrRuO₃ show.

Chiral anomaly in the quantum limit

We carried out the angle-dependent magnetotransport measurements for the SrRuO₃ film with $t = 10$ nm (Fig. 3). Figure 3a shows the angular dependence of MR ($(\rho_{xx}(B) - \rho_{xx}(0T))/\rho_{xx}(0T)$) for the SrRuO₃ film with $t = 10$ nm at 2 K measured by the PPMS (up to 14 T). Here, B is rotated from the out-of-plane [001] direction of the SrTiO₃ substrate ($\theta = 90^\circ$) to the in-plane direction parallel to the current ($\theta = 0^\circ$). The rotation angle θ is defined in the inset of Fig. 3a. As has been already described in the “Thickness-dependent

magnetotransport” section, the unsaturated linear positive MR is observed when B is applied perpendicular to the current I ($\theta = 90^\circ$); note that quantum oscillations are superimposed onto the data. With decreasing θ , the sign of the MR changes from positive to negative, and the negative MR ratio is enhanced. The negative MR at $\theta \leq 30^\circ$ becomes linear above 5 T (Fig. 3a). In ferromagnetic SrRuO₃, the time-reversal-symmetry breaking lifts the spin degeneracy and leads to linear crossing of non-degenerate bands at many k points, resulting in a pair of Weyl nodes with opposite chiralities (L and R; Fig. 3c)^{27,32}. In the presence of a magnetic field, the Landau quantization of a pair of Weyl nodes with opposite chiralities occurs (Fig. 3d, e). In Fig. 3d, e, B_{QL} represents the magnetic field at which the quantum limit is reached and all the Weyl fermions occupy the zeroth Landau levels. When $B < B_{QL}$ (Fig. 3d), nonorthogonal electric and magnetic fields ($\mathbf{E} \cdot \mathbf{B} \neq 0$) lead to the chiral charge transfer between the two Landau levels with opposite chiralities^{62,63}. In the weak- B limit ($B < B_{QL}$; Fig. 3d), calculations based on the semiclassical Boltzmann theory predict that time-reversal-symmetry-breaking Weyl semimetals (magnetic Weyl semimetals) show a negative MR that is linear in the projection component of B in the direction of ^{54,63,64}, in contrast to the quadratic dependence expected for space-inversion symmetry breaking Weyl semimetals^{19,21,65}. Thus, the linear negative MR observed for $\theta \leq 30^\circ$ and $5 \leq B \leq 14$ T when rotating B from orthogonal to parallel to I (Fig. 3a) is consistent with a chiral anomaly in magnetic Weyl semimetals²⁷. In our previous study²⁷, similar chiral-anomaly-induced negative MR has been observed for the SrRuO₃ film with $t = 63$ nm.

To verify the negative MR stemming from the chiral anomaly, we carried out high-field angle-dependent magnetotransport measurements using the mid-pulse magnet up to 52 T. This is of importance because the negative MR at low field in Weyl semimetals can be also brought about by experimental artifacts and impurities^{65–67}. Therefore, observing the behavior of the negative MR in the quantum limit (Fig. 3e), where the chiral-anomaly-induced negative MR is predicted to saturate^{21,65,68}, is necessary. Figure 3b shows the angular dependence of the high-field magnetotransport for $t = 10$ nm at 0.7 K with B rotated from the out-of-plane [001] direction of the SrTiO₃ substrate to the in-plane direction parallel to the current. As in the case of the PPMS measurements up to 14 T (Fig. 3a), the sign of the MR at high fields changes from positive to negative with decreasing θ (Fig. 3b). Importantly, the negative MR with $\theta = 5.3^\circ$ saturates above 30 T

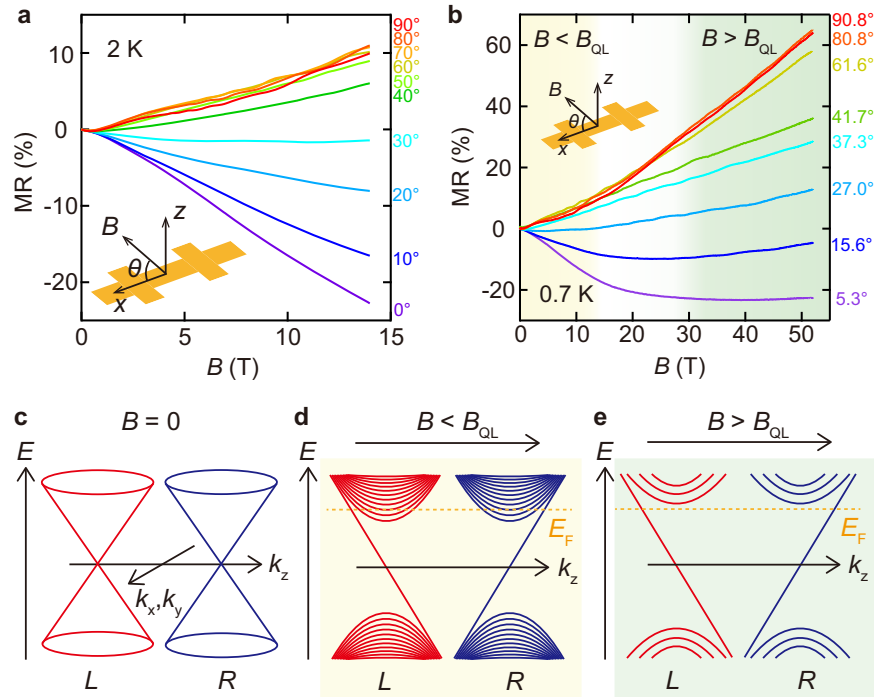


Fig. 3 Angle-dependent magnetotransport for the SrRuO₃ film with $t = 10$ nm and Landau quantization of a pair of Weyl nodes. **a** Angular dependence of MR $(\rho_{xx}(B) - \rho_{xx}(0 T)) / \rho_{xx}(0 T)$ for the SrRuO₃ film with $t = 10$ nm at 2 K, measured by the PPMS up to 14 T. **b** Angular dependence of MR $(\rho_{xx}(B) - \rho_{xx}(0 T)) / \rho_{xx}(0 T)$ for the SrRuO₃ film with $t = 10$ nm at 0.7 K, measured by the mid-pulse magnet up to 52 T. **c** Schematic diagram of a pair of Weyl nodes with opposite chiralities (L and R) with $B = 0$. **d**, **e** Schematic diagram of Landau levels of a pair of Weyl nodes with $B < B_{QL}$ and $B > B_{QL}$, respectively, where B_{QL} is the magnetic field at which the quantum limit is reached. In **b**, beige and green areas indicate $B < B_{QL}$ and $B > B_{QL}$ range, respectively.

(Fig. 3b), confirming that the negative MR originates from the chiral anomaly. In the quantum limit (Fig. 3e), the conductivity when B is parallel to l is expressed by

$$\sigma_{xx} = N_W \frac{e^2 v_F}{4\pi\hbar l_B^2} \tau_{\text{inter}}(B), \quad (1)$$

where N_W is the number of Weyl points in the Brillouin zone, e is the elementary charge, \hbar is the Dirac constant, v_F is the Fermi velocity, $l_B = \sqrt{\hbar/eB}$ is the magnetic length, and $\tau_{\text{inter}}(B)$ is the field-dependent inter-nodal scattering time^{62,68}. In the quantum limit of Weyl semimetals, the scattering rate $1/\tau_{\text{inter}}(B)$ is predicted to increase roughly in proportion to B under the assumption of short-range impurity scattering, and the scattering factor cancels the factor of l_B^2 in Eq. (1), resulting in the B -independent conductivity^{65,68,69}. Indeed, the saturation of the chiral-anomaly-induced negative MR above the quantum limit ($B > B_{QL}$) has been observed in typical Weyl semimetals Na₃Bi²¹ and TaAs⁶⁵ as an inherent property of Weyl fermions, although it has not been observed in magnetic Weyl semimetals. Nonetheless, our observation of the saturation of the negative MR when B is parallel to l is consistent with the theoretically predicted behavior for the chiral anomaly in magnetic Weyl semimetals.

The tilting of the Weyl nodes is an important feature that characterizes Weyl semimetals. The calculated band structures for a set of selected Weyl nodes in the vicinity of the Fermi level are shown in Fig. 4 (see Methods section “First-principles calculations” for details). According to our calculations, the tilt of the linear band crossings is small and preserves an elliptical Weyl cone with the point-like Fermi surface. As shown in previous theoretical studies⁶⁴, tilting of the Weyl nodes can result in a one-dimensional chiral anomaly, which in turn shows linear negative MR. Therefore, our electronic structure calculations suggest that the observed linear negative MR below the quantum limit originates from the

one-dimensional chiral anomaly as a distinct feature of time-reversal symmetry broken (e.g., magnetic) Weyl semimetals.

In principle, the chiral anomaly induced negative MR should be accompanied by SdH oscillations originating from the bulk three-dimensional Weyl fermions, because the chiral anomaly stems from the Landau quantization of the bulk three-dimensional Weyl fermions. However, oscillations originating from the bulk three-dimensional Weyl fermions were not clear in the SrRuO₃ samples studied here, as will be described in the “High-mobility two-dimensional carriers” section. Since the Landau levels could be broadened by impurity scattering, disorder in the crystals, if any, readily hampers the observation of clear quantum oscillations^{70,71}. In fact, in Dirac semimetal Na₃Bi and zero-gap semiconductor GdPtBi, chiral-anomaly-induced MR without quantum oscillations of the bulk three-dimensional Weyl fermions has been reported⁷². Accordingly, further improvement in the crystallinity of SrRuO₃ is required to observe clear SdH oscillations of the bulk three-dimensional Weyl fermions, which will allow for detailed characterization of the Fermi surface. For instance, using a substrate having smaller lattice mismatch with SrRuO₃, e.g. DyScO₃ and Sr_{1-x}Ba_xTiO₃, appears to be a promising means since the SrRuO₃ film on the DyScO₃ substrate has fewer defects owing to the smaller lattice mismatch⁷³.

High-mobility two-dimensional carriers

To study the dimensionality of the SdH oscillations, we investigated their angular dependence in the SrRuO₃ film with $t = 10$ nm (Fig. 5; see Methods section “Fourier transformation analysis for SdH oscillations” for details). The SdH oscillations are observed from $\theta = 90^\circ$ to 30° , but not for θ ranging from 20° to 0° (Fig. 5a). This behavior of weakened oscillations with decreasing θ down to the in-plane direction is a typical feature of two-dimensional carriers^{6,12,74}. As shown in Fig. 5b, the peak frequency F of the FFT spectra gradually shifts from ~ 25 T to a high

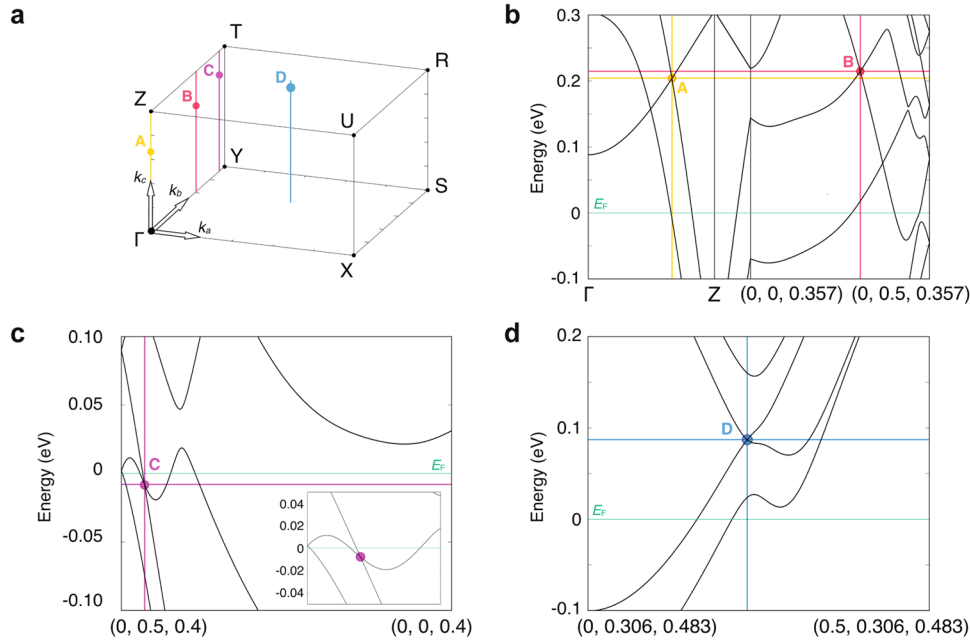


Fig. 4 Selected Weyl nodes (A–D) in the vicinity of the Fermi level in orthorhombic SrRuO₃. **a** Position of the Weyl nodes in the irreducible part of the Brillouin zone. Vertical yellow, red, pink, and blue lines indicate the in-plane (Γ –X–S–Y plane) positions of the Weyl nodes for easy viewing. The Weyl nodes are given in fractional coordinates as A = (0, 0, 0.332), B = (0, 0.307, 0.357), C = (0, 0.464, 0.4), and D = (0.233, 0.306, 0.483). **b–d** Band structures for the ferromagnetic ground state with spin–orbit coupling as obtained from GGA + U calculations with $U = 2.6$ eV and $J = 0.6$ eV. In **b–d**, the intersection of the straight lines represents the Weyl nodes. E_F stands for the Fermi level.

frequency with B rotated from $\theta = 90^\circ$ to 30° . The frequency is well described by a $1/\cos(90^\circ - \theta)$ dependence, as shown later (Fig. 6c), indicating that the field component perpendicular to the surface is relevant for the cyclotron orbit. This angular dependence is a hallmark of two-dimensional carriers^{6,10,12,74}. As shown in Fig. 5d, e, we also measured the temperature dependence of the SdH oscillations and estimated the effective cyclotron mass m^* according to the Lifshitz-Kosevich theory at each angle as follows:^{9,27,75,76}

$$\Delta\sigma_{xx} \propto \frac{T}{\sinh(aT)}, \quad (2)$$

where $a = \frac{2\pi^2 k_B m^*}{\hbar e B}$, k_B is the Boltzmann constant, and \bar{B} is defined as the average inverse field of the FFT interval. The estimated m^* at $\theta = 90^\circ$ is $0.25m_0$ (m_0 : the free electron mass in a vacuum) (Fig. 5c). We also determined the Dingle temperature T_D from the Lifshitz-Kosevich theory (see the Sec. II of the supplementary information) and obtained the quantum mobility $\mu_q = e\hbar/(2\pi k_B m^* T_D) = 3.5 \times 10^3 \text{ cm}^2/\text{Vs}$. These results confirm the existence of the high-mobility two-dimensional carriers with a light cyclotron mass in the SrRuO₃ film with $t = 10$ nm. The F and m^* values ($F \sim 25$ T and $m^* = 0.25m_0$) of the SrRuO₃ film with $t = 10$ nm are, respectively, the same as and comparable to those of the main component of the SdH oscillations in the SrRuO₃ film with $t = 63$ nm ($F \sim 26$ T and $m^* = 0.35m_0$) reported previously²⁷. Notably, the μ_q value of the SrRuO₃ film with $t = 10$ nm is about one third of that in the SrRuO₃ film with $t = 63$ nm ($\mu_q = 9.6 \times 10^3 \text{ cm}^2/\text{Vs}$). The reduced μ_q value in the former film suggests that disorder near the interface between SrRuO₃ and SrTiO₃ substrate is the dominant scattering mechanism, which shortens the quantum lifetime of the high mobility two-dimensional carriers in the SrRuO₃ film with $t = 10$ nm. This disorder may be the origin of the short-range scattering mechanism postulated in the theory of the saturation of the negative MR in the quantum limit^{65,68,69}.

As confirmed in Fig. 5a, the SdH oscillation amplitude up to 14 T ($=0.071 \text{ T}^{-1}$) becomes small at lower angles, and it is difficult to

follow the frequency. To further scrutinize the quantum oscillations, especially at lower angles ($\theta \leq 30^\circ$), we analyzed the SdH oscillations using the mid-pulse magnet up to 52 T in the SrRuO₃ film with $t = 10$ nm (Fig. 6). Except for 5.3° , the SdH oscillations can be clearly seen at each angle. At $\theta = 90.8^\circ$ and 80.8° , the SdH oscillations are distinct between the two $1/B$ ranges (Fig. 6a): the high $1/B$ range from 0.035 to 0.1 T^{-1} and the low $1/B$ range from 0.018 to 0.035 T^{-1} . The SdH oscillation at $\theta = 90.8^\circ$ in the high $1/B$ range has the frequency $F \sim 25$ T, which corresponds to the Weyl fermions with the high μ_q and light m^* observed in Fig. 5. The other oscillation has a high frequency of $F \sim 300$ T and the cyclotron mass m^* of $2.4m_0$ (see the Sec. IV of the supplementary information). These F and m^* values are consistent with those of the trivial Ru 4d band that crosses E_F , which were reported in an early de Haas–van Alphen measurement⁶¹ and an SdH measurement using a standard lock-in technique at 0.1 K up to 14 T²⁷. Since our focus is not on the trivial Ru 4d orbit in the low $1/B$ range but on the Weyl fermions, the data in the low $1/B$ range was excluded from the data for $\theta = 90.8^\circ$ and 80.8° for the FFT analysis. As in the case of the PPMS measurements, the SdH peak frequency gradually shifts to a high frequency with decreasing θ from 90.8° to 15.6° in Fig. 6b, c. In Fig. 6a, the quantum limit, which is the inverse value of the FFT frequency, is indicated by black arrows. Since the FFT frequencies at high angles ($\theta \geq 61.6^\circ$) are below the highest applied magnetic field of 52 T, we can observe the quantum limit as evidenced by the disappearance of the SdH oscillations of the two-dimensional carriers in the high- B region above the SdH frequencies. The frequency obtained by the high-field measurements is also well fitted by $1/\cos(90^\circ - \theta)$; Fig. 6c, as is the case in the PPMS measurements.

We also measured the SdH oscillations for the Weyl fermions in the SrRuO₃ film with $t = 10$ nm at 0.7 K using a long-pulse magnet up to 40 T (Supplementary Fig. 6), which allows for a more accurate measurement of resistivity because measurement time is longer than that of the mid-pulse magnet up to 52 T. Since the SdH oscillations are clearly observed from low magnetic fields by improved measurement accuracy, the spectra of the Fourier

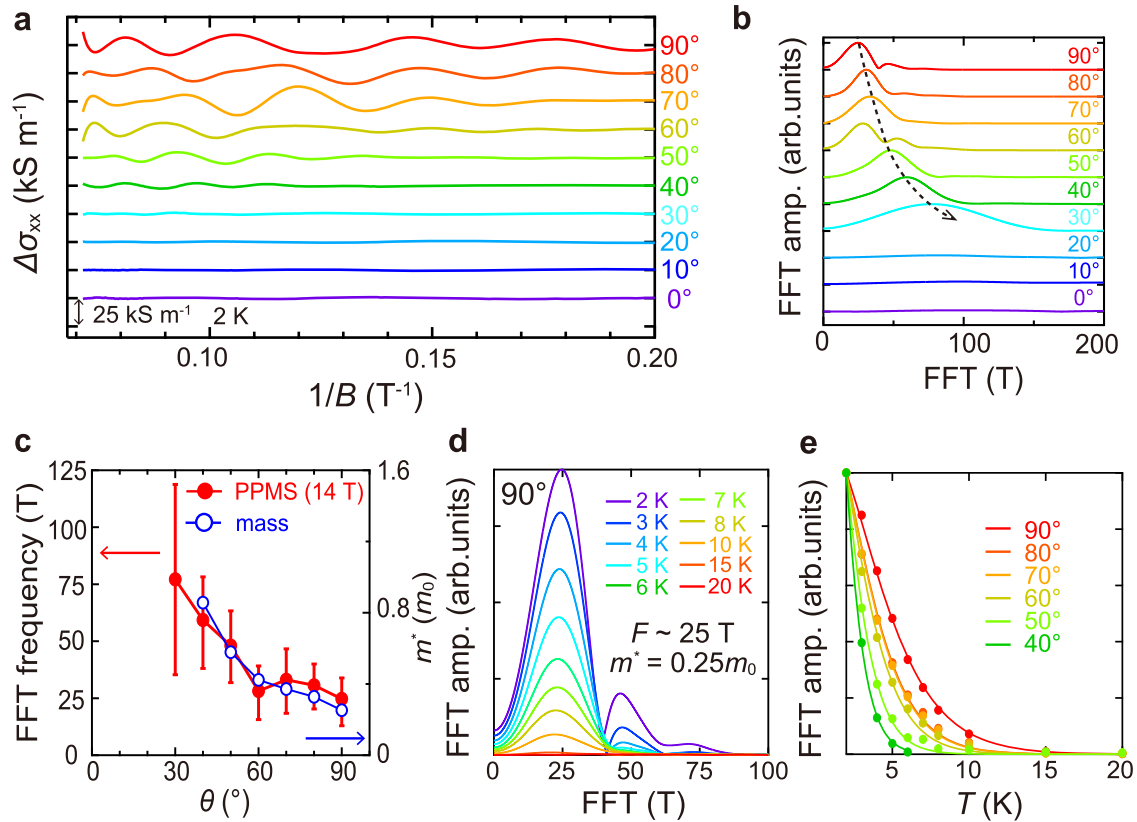


Fig. 5 Angular dependence of the SdH oscillations for the SrRuO₃ film with $t = 10$ nm using the PPMS. **a** Angular dependence of the background-subtracted SdH oscillations at 2 K with B ($5 \text{ T} < B < 14 \text{ T}$) for the SrRuO₃ film with $t = 10$ nm. **b** Angular dependence of the FFT spectra of SdH oscillations at 2 K for the film with $t = 10$ nm. The dashed line is a guide for the peak shift. **c** Angular dependence of the FFT frequency (red filled circles) and the cyclotron mass (blue open circles). **d** Temperature dependence of the Fourier transform spectra of SdH oscillations at $\theta = 90^\circ$ for the SrRuO₃ film with $t = 10$ nm. **e** Temperature dependence of the FFT amplitude from $\theta = 90^\circ$ to 40° for mass estimations according to the Lifshitz-Kosevich theory.

transform have sharper peaks than those obtained by the PPMS and the mid-pulse magnet measurements, as shown in Supplementary Fig. 6b. All the results from PPMS, mid-, and long-pulse magnet measurements converge and are well fitted with an angular-dependence curve for two-dimensional carriers (Fig. 6c), strongly indicating the existence of the two-dimensional Weyl fermions in the SrRuO₃ film with $t = 10$ nm. Altogether, the existence of high-mobility two-dimensional carriers, which had never been observed in ferromagnets, is established in the epitaxial ferromagnetic oxide SrRuO₃.

Origin of the two-dimensional carriers: surface Fermi arcs

Possible origins of the high-mobility two-dimensional carriers in Weyl semimetals are the surface Fermi arcs (Fig. 7) and the quantum confinement of the three-dimensional Weyl fermions^{8–15,77}. The SdH oscillations mediated by the surface Fermi arcs and the quantum confinement appear when the film is thinner than the mean free path and the Fermi wavelength of carriers, respectively^{6,12,77}. The mean free path $\hbar^2 k_F / (2\pi k_B m^* T_D)$ and the Fermi wavelength $2\pi/k_F$ obtained by the SdH oscillations of the high-mobility two-dimensional carriers for the SrRuO₃ film with $t = 10$ nm in Fig. 5a are ~ 65.4 and ~ 22.4 nm, respectively. Here, k_F is the Fermi wave number. Hence, the film thickness of 10 nm satisfies both conditions. In the SrRuO₃ film with $t = 63$ nm, the mean free path and the Fermi wavelength of the main component of the SdH oscillations are ~ 179 and ~ 22.4 nm, respectively²⁷. To determine the origin of the two-dimensional quantum transport, we also studied the angular dependence of the SdH oscillations in the SrRuO₃ film with $t = 63$ nm, which is

thinner than the mean free path but thicker than the Fermi wavelength. We note that, in Dirac semimetal Cd₃As₂, suppression of backscattering, which results in a transport lifetime 10^4 times longer than the quantum lifetime, has been reported⁷⁸. Therefore, the mean free path estimated by quantum lifetime may also be underestimated in SrRuO₃. Figure 8 shows the angular dependence of the SdH oscillations in the SrRuO₃ film with $t = 63$ nm. As in the case of the SrRuO₃ thin film with $t = 10$ nm, the peak frequency of the FFT spectra gradually shifts to a higher frequency with decreasing θ from 90° to 10° in Fig. 8b. The frequency also shows the two-dimensional $1/\cos(90^\circ - \theta)$ dependence, with the exception of that at $\theta = 0^\circ$ (Fig. 8c), indicating that the SdH oscillations at θ from 90° to 10° come from the two-dimensional high mobility carriers. This result suggests that the high mobility two-dimensional carriers possibly come from the surface Fermi arcs, not from the quantum confinement effect. In contrast, the SdH peak frequency of 64 T at $\theta = 0^\circ$ is outside the above two-dimensional trend, indicating that these SdH oscillations are different from those of the high mobility two-dimensional carriers. Additionally, for $\theta \geq 40^\circ$, small FFT peaks are also discernible, e.g., at ~ 44 T for $\theta = 90^\circ$ (black solid arrows in Fig. 8b). These peaks and their weak angular dependencies possibly come from the orbit of the bulk three-dimensional Weyl fermions. Since the SdH oscillations from the surface Fermi arcs are connected via the Landau quantization of the bulk three-dimensional Weyl fermions⁷⁷, further improvement in the crystallinity of SrRuO₃ will allow for detailed characterization of the SdH of the bulk Weyl fermions and their relevance to the surface Fermi arcs.

The thickness-dependent phase shift of the SdH oscillations will provide essential evidence for the non-trivial nature of the SdH

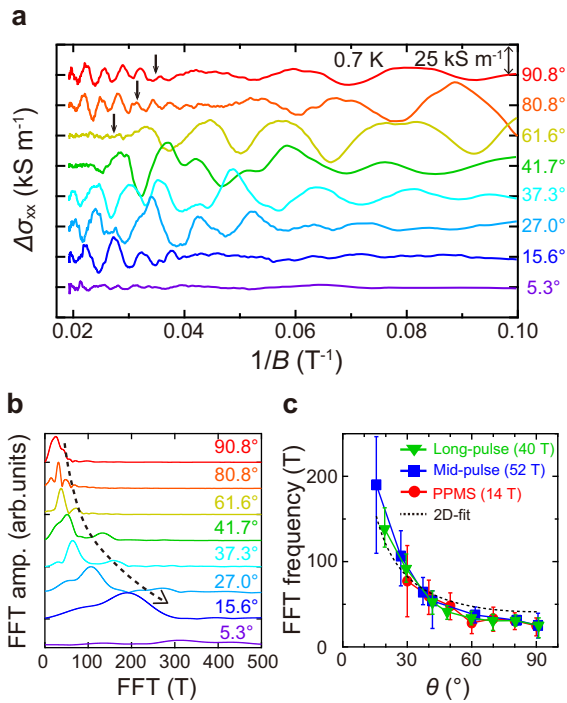


Fig. 6 Angular dependence of the SdH oscillations for the SrRuO₃ film with $t = 10$ nm using the mid-pulse magnets. **a** Angular dependence of the background-subtracted SdH oscillations at 0.7 K with B ($10 \text{ T} < B < 52 \text{ T}$) for the SrRuO₃ film with $t = 10$ nm, measured by the mid-pulse magnet. These spectra were smoothed (see the Sec. III of the supplementary information). The arrows indicate the quantum limit, which is the inverse value of the FFT frequency in **c**. **b** Angular dependence of the FFT spectra of SdH oscillations at 0.7 K for the film with $t = 10$ nm. The dashed line is a guide for the peak shift. **c** Angular dependence of the FFT frequency. Here, the data obtained by the long-pulse magnet are also shown. The dashed line is the fitting of a two-dimensional angular dependence ($\sim 1/\cos(90^\circ - \theta)$).

oscillations mediated by the surface Fermi arcs. According to the semiclassical analysis of the closed magnetic orbit, called Weyl orbit^{79–82}, formed by connecting the surface Fermi arcs via the Weyl nodes in bulk^{10,77}, the thickness t dependence of the position of the N th conductivity maximum B_N is expressed by

$$B_N^{-1} = ek_0^{-1} \left(\frac{(N + \gamma)\pi v_F}{E_F} - \frac{t}{\hbar} \right), \quad (3)$$

where k_0 , γ , v_F , and E_F are the length of the surface Fermi arc in reciprocal space, the sum of a constant quantum offset and the Berry phase, the Fermi velocity, and the Fermi energy. We note that it is assumed that identical Fermi arcs are on the top and bottom surfaces in Eq. (3)⁸³. Equation (3) describes that the inverse of the SdH oscillation frequency $1/F = B_N^{-1} - B_{N-1}^{-1}$ and the thickness-dependent phase shift $\beta(t)$ of the SdH oscillation are given by $ek_0^{-1} \left(\frac{\pi v_F}{E_F} \right)$ and $\frac{E_F t}{\pi v_F \hbar}$, respectively. Thus, the SdH oscillation originating from Weyl orbits can be expressed by

$$\Delta\sigma_{xx} \propto \cos \left[2\pi \left(\frac{F}{B} + \gamma + \beta(t) \right) \right] \quad (4)$$

It is apparent from these equations that the phase shift $\beta(t)$ of the SdH oscillations mediated by the surface Fermi arcs has a linear relation with t . To examine this non-trivial phase shift, we carried out the Landau level (LL) fan diagram analyses for the conductivity maximum of the SdH oscillations with various thicknesses. Figure 9 shows the background-subtracted SdH oscillations at 2 K with B ($3.3 \text{ T} < B < 14 \text{ T}$) applied in the out-of-

plane [001] direction of the SrTiO₃ substrate for the SrRuO₃ films with $t = 10, 20, 40,$ and 60 nm. The FFT frequencies F ($= 27, 26, 25,$ and 34 T for $t = 10, 20, 40,$ and 60 nm, respectively) are determined from the peak positions of the FFT spectra of the SdH oscillations from 5 to 14 T. We extracted the magnetic field B_N of the N th conductivity maximum, and estimated the phase shift $\gamma + \beta(t)$ from the LL fan diagram for the conductivity maximum with a fixed slope of F (Fig. 10). As expected from Eqs. (3) and (4), we can see the linear relation between the $\beta(t)$ and t (Fig. 10e) as a distinguished non-trivial nature of the SdH oscillations mediated by the surface Fermi arcs. The linear thickness dependence of the shift of the SdH oscillations verifies that the high-mobility two-dimensional carriers come from the surface Fermi arcs (Fig. 7), not from the trivial origins such as quantum confinement effect, trivial 2D gas on the surface of the film, anisotropic bulk Fermi surface, etc.

From the $1/F = ek_0^{-1} \left(\frac{\pi v_F}{E_F} \right)$ value and the slope of the phase shift $\frac{E_F}{\pi v_F \hbar}$ of the SdH oscillation of the Weyl orbit, we can determine the $\frac{E_F}{v_F}$ and k_0 values. The estimated $\frac{E_F}{v_F}$ and k_0 values are $2.92 \times 10^{-8} \text{ eVs/m}$ and 2.8 nm^{-1} , respectively. Since the length of the surface Fermi arc is not much smaller than the size of the pseudocubic Brillouin zone $\frac{2\pi}{a} = 15.98 \text{ nm}^{-1}$ of SrRuO₃, our findings will stimulate a challenge for its observation by angle-resolved photoemission spectroscopy. In addition, we can determine the γ value from the extrapolation of the t dependence of the $\gamma + \beta(t)$ to $t = 0$. The obtained γ value is -0.16 .

DISCUSSION

We have systematically studied quantum oscillations observed in high-quality SrRuO₃ films and successfully detected high-mobility two-dimensional carriers with light cyclotron mass, which possibly comes from the surface Fermi arcs. We also observed the saturation of the negative MR in the quantum limit, which is strong evidence of the chiral anomaly. These are the first observations of two-dimensional high-mobility carriers and chiral-anomaly-induced negative MR in the quantum limit in magnetic Weyl semimetals and magnetic oxides. The interface with the SrTiO₃ substrate and the surface of the SrRuO₃ films might be subject to slight structural differences, such as octahedral distortion and rotation^{84–87}. However, our previous band structure calculations showed that a slight distortion induced by the substrate does not significantly change the band structure of SrRuO₃ and that Weyl points are robust with the distortion as long as the band inversion is present²⁷. In addition, generally, magnetic anisotropy in magnetic Weyl semimetals should affect angle-dependent MR originating from the quantum transport of Weyl fermions since the distribution of Weyl nodes in magnetic Weyl semimetals is determined by the magnetic arrangement²⁷. Especially in SrRuO₃ films, the magnetic anisotropy can be controlled via epitaxial strain, and therefore, SrRuO₃ will be a platform for exploring the relationship between magnetic anisotropy, quantum transport properties of Weyl fermions, and chiral-anomaly-induced negative MR. The knowledge gained through such study will be helpful for controlling those properties by magnetization switching in future.

Our findings provide a foundation for studying exotic quantum transport phenomena in magnetic Weyl semimetals embedded in oxide heterostructures. Perovskite oxides that can be epitaxially grown with SrRuO₃ include those with various physical properties such as insulators (e.g. SrTiO₃)⁴¹, metals (e.g. Nb:SrTiO₃)⁴¹, ferroelectrics (e.g. BaTiO₃)⁴¹, and superconductors (e.g. Sr₂RuO₄)⁸⁸. Utilizing magnetic Weyl states in these epitaxial heterostructures may enable functionalities^{89,90} and thus widen the accessible oxide electronics devices. In addition, the emergence of the hitherto hidden two-dimensional Weyl states in a ferromagnet is an essential step toward realizing the intriguing quantum Hall

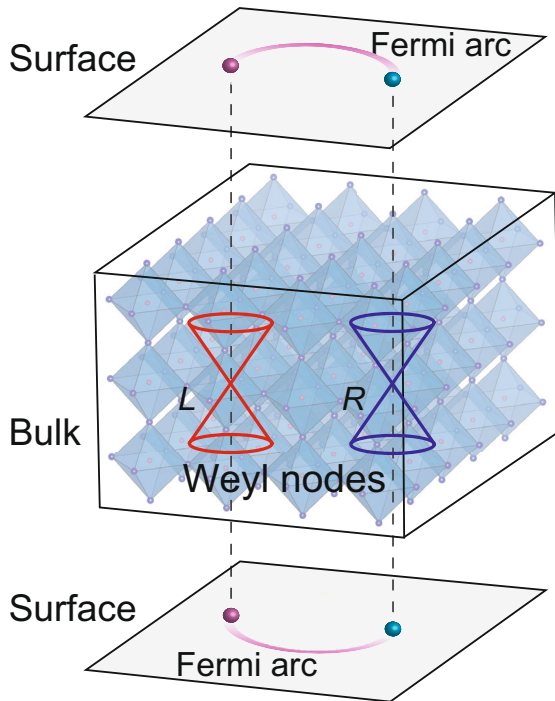


Fig. 7 Schematic diagram of a pair of Weyl nodes with opposite chiralities (L and R) and surface Fermi arcs in SrRuO_3 . The pink curves represent surface Fermi arcs connecting the projections of the bulk Weyl nodes.

effect, which should be controllable through magnetization switching.

Note added: we became aware of a recent preprint⁹¹, which was uploaded later than the preprint of this article (arXiv:2106.03292), that report similar 2D-like SdH oscillations with a frequency of ~ 30 T. From the nonmonotonic thickness dependence on the FFT amplitude, they also argued the SdH oscillation with a frequency of ~ 30 T is more likely to be surface origin.

METHODS

Sample preparation

We grew high-quality epitaxial SrRuO_3 films with thicknesses $t = 10, 20, 40, 60,$ and 63 nm on (001) SrTiO_3 substrates (Fig. 1a) in a custom-designed MBE setup equipped with multiple e-beam evaporators for Sr and Ru^{27,47}. The SrRuO_3 films were prepared at the Ru flux = 0.365 \AA s^{-1} , growth temperature = 781°C , and O_3 -nozzle-to-substrate distance = 15 mm. These conditions are the same as those in ref. ²⁷. The growth parameters, such as the growth temperature, supplied Ru/Sr flux ratio, and oxidation strength, were optimized by Bayesian optimization, a machine-learning technique for parameter optimization^{47,49,50}, with which we achieved a high residual resistivity ratio (RRR) of 19.2 and 81.0 with $t = 10$ and 63 nm, respectively. We precisely controlled the elemental fluxes by monitoring the flux rates with an electron-impact-emission-spectroscopy sensor, and the stoichiometric Sr/Ru ratio of a SrRuO_3 film was confirmed using energy dispersive x-ray spectroscopy⁹². Figure 1b shows the θ - 2θ XRD patterns around the (002) pseudocubic diffractions of the SrRuO_3 film with $t = 63$ nm. Laue fringes in the θ - 2θ XRD pattern indicate high crystalline quality and a large coherent volume of the film. The out-of-plane lattice constant, estimated from the Nelson-Riley extrapolation method⁹³, was 3.950 \AA , $\sim 0.5\%$ larger than the pseudocubic lattice constant of the bulk specimens (3.93 \AA)⁴¹. This indicates that the SrRuO_3 film is compressively strained due to the

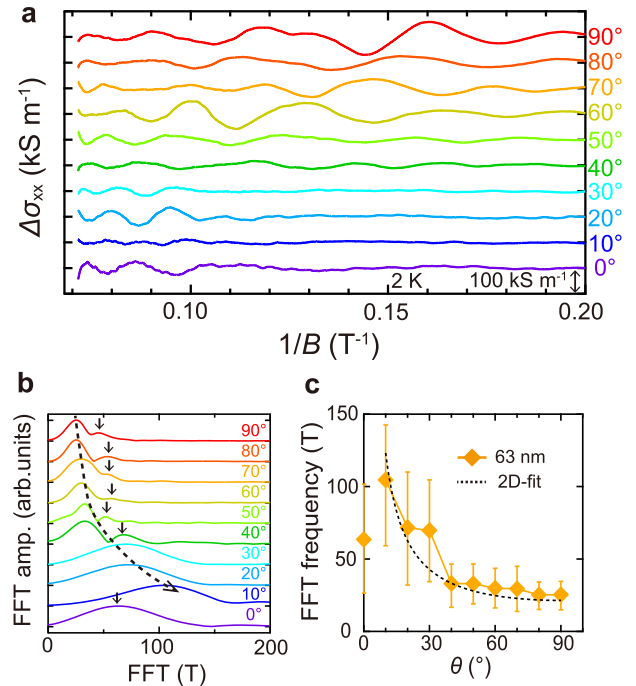


Fig. 8 Angular dependence of the SdH oscillations for the SrRuO_3 film with $t = 63$ nm. **a** Angular dependence of the background-subtracted SdH oscillations at 2 K with B ($5 \text{ T} < B < 14 \text{ T}$) for the SrRuO_3 film with $t = 63$ nm. **b** Angular dependence of the FFT spectra of SdH oscillations at 2 K for the film with $t = 63$ nm. The dashed line is a guide for the peak shift of the two-dimensional Weyl fermions. Black solid arrows indicate the peak positions of the three-dimensional Weyl fermions. **c** Angular dependence of the FFT frequency. The dashed line is the fitting of a two-dimensional angular dependence ($\sim 1/\cos(90^\circ - \theta)$).

lattice constant of the SrTiO_3 substrate (3.905 \AA) being $\sim 0.6\%$ smaller than the pseudocubic lattice constant of SrRuO_3 . The AFM images show the surface morphology composed of flat terraces and molecular steps with height of ~ 0.4 nm, corresponding to a single unit cell thickness (Fig. 1c, d). The root-mean-square roughness is 0.17 nm, indicating that the SrRuO_3 film has an atomically smooth surface. The SrRuO_3 film with $t = 63$ nm has an orthorhombic structure with two-fold in-plane symmetry, as evidenced by the XRD ϕ scans in our previous study⁷³. Epitaxial growth of the high-quality single-crystalline SrRuO_3 film with an abrupt substrate/film interface is seen in EELS-STEM images (Fig. 1e). Further information about the MBE setup, preparation of the substrates, and sample properties are described elsewhere^{27,53,94–96}.

Magnetotransport measurements

We fabricated the Hall bar structures (length $l = 350 \mu\text{m}$, width $w = 200 \mu\text{m}$; Fig. 1f) by photolithography and Ar ion milling. We deposited Ag electrodes on a SrRuO_3 surface before making the Hall bar structure. Magnetotransport up to 14 T was measured in a DynaCool physical property measurement system (PPMS) sample chamber equipped with a rotating sample stage. High-field magnetotransport measurements up to 52 T and 40 T were performed using a non-destructive mid-pulse magnet with a pulse duration of 36 ms and long-pulse magnet with a pulse duration of 1.2 s, respectively, at the International MegaGauss Science Laboratory at the Institute for Solid State Physics, the University of Tokyo⁹⁷.

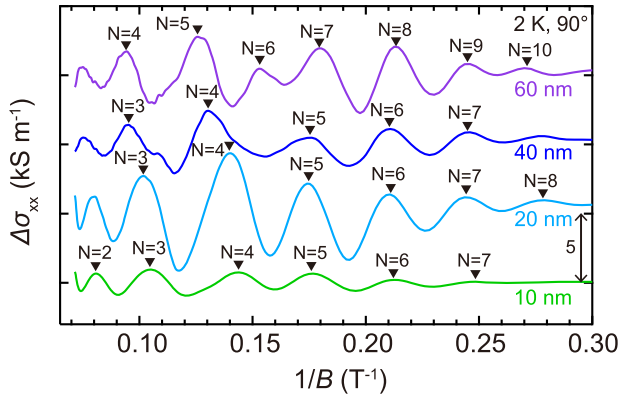


Fig. 9 Background-subtracted SdH oscillations at 2 K with B ($3.3 \text{ T} < B < 14 \text{ T}$). The magnetic field was applied in the out-of-plane [001] direction of the SrTiO₃ substrates for the SrRuO₃ films with $t = 10, 20, 40,$ and 60 nm . The black triangles show peak positions.

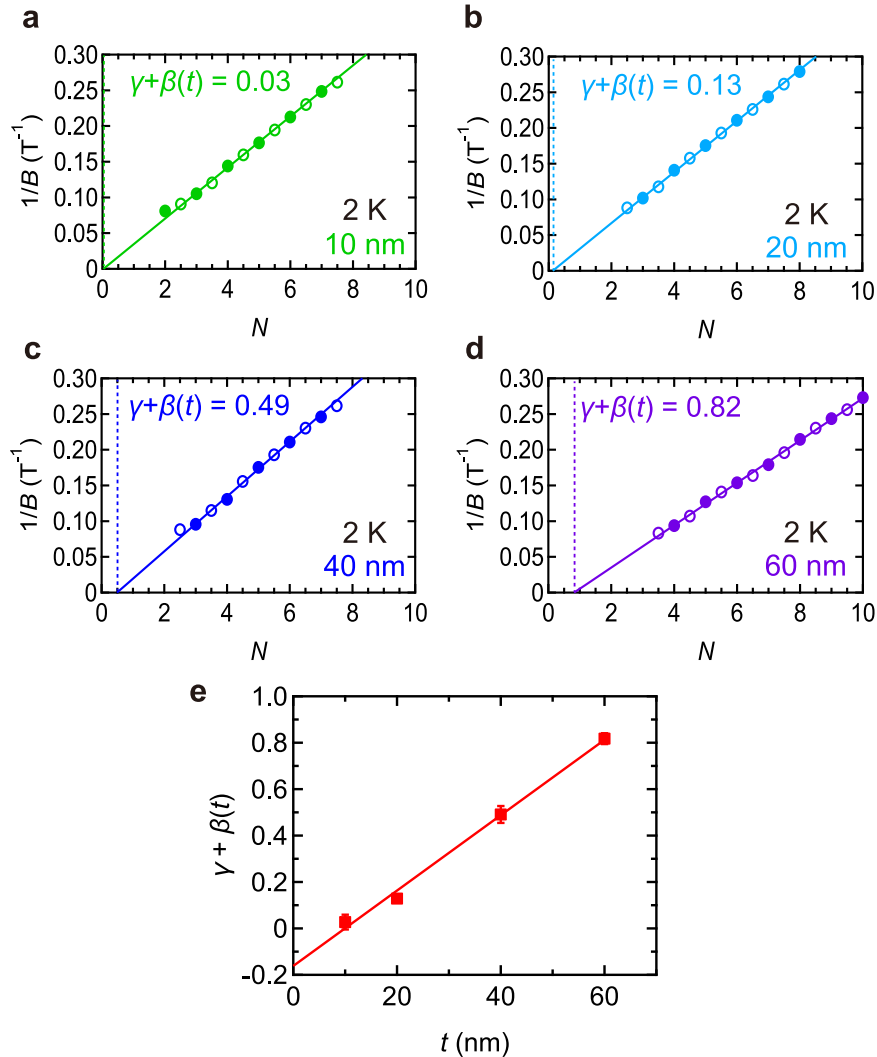


Fig. 10 Thickness t dependence of the LL fan diagram of the conductivity maximum for the SrRuO₃ films. **a** $t = 10 \text{ nm}$, **b** 20 nm , **c** 40 nm , and **d** 60 nm . The fixed slopes of the linear fittings are obtained by the frequency F . All plotted data points were used in the linear fittings. $\gamma + \beta(t)$ is the phase shift in Eq. (4). **e** Thickness t dependence of the $\gamma + \beta(t)$. The red line represents the linear fitting. The error bars are defined as the standard deviation of the linear fittings in **a-d**.

First-principles calculations

Electronic structure calculations were performed within density functional theory by using generalized gradient approximation⁹⁸ for the exchange correlation functional in the projector-augmented plane wave formalism⁹⁹ as implemented in the Vienna Ab-initio Simulation Package¹⁰⁰. The energy cutoff was set to 500 eV, the Brillouin zone was sampled by an $8 \times 8 \times 6$ Monkhorst-Pack mesh¹⁰¹, and the convergence criterion for electronic density was put to 10^{-8} eV. Experimental crystal structure of orthorhombic SrRuO₃ was adopted for all calculations (the $Pbnm$ space group, $a = 5.567 \text{ \AA}$, $b = 5.5304 \text{ \AA}$, $c = 7.8446 \text{ \AA}$)⁴¹. The calculations were performed for the ferromagnetic state with spin-orbit coupling. The effect of electronic correlations in the Ru 4d shell was considered by using the rotationally invariant GGA + U scheme¹⁰² with $U = 2.6 \text{ eV}$ and $J = 0.6 \text{ eV}$.

For numerical identification of the Weyl nodes, the electronic band structure was interpolated with the maximally localized Wannier functions by projecting the bands near the Fermi level

onto the Ru d atomic orbitals, as implemented in the wannier90 package¹⁰³. Band crossings in the reciprocal space were calculated by steepest-descent optimization of the gap function, $\Delta = (E_{n+1,k} - E_{n,k})^2$, on a uniform mesh for the Brillouin zone up to $25 \times 25 \times 25$ ¹⁰⁴. The two bands are considered degenerate when the gap is below the threshold of 10^{-5} eV. The results of such electronic structure calculations and the full set of the Weyl points in the vicinity of the Fermi level were reported in our previous study²⁷.

Fourier transformation analysis for SdH oscillations

We measured the longitudinal resistance R_{xx} and Hall resistance R_{xy} of the Hall bar patterned SrRuO₃ films (width $w = 200 \mu\text{m}$, length $l = 350 \mu\text{m}$). The longitudinal resistivity $\rho_{xx} = R_{xx}wt/l$ and Hall resistivity $\rho_{xy} = R_{xy}t$ were obtained from the R_{xx} and R_{xy} values. From ρ_{xx} and ρ_{xy} , we obtained the longitudinal conductivity $\sigma_{xx} = \rho_{xx}/(\rho_{xx}^2 + \rho_{xy}^2)$ of the conductivity tensor. We subtracted the background of the conductivity from the σ_{xx} data (see the Sec. VI of the supplementary information) using a polynomial function up to the eighth order and extracted the oscillation components. For the Fourier transformation, we interpolated the data in Figs. 5a, 6a, 8a, and 9, and Supplementary Fig. 6a to prepare equally spaced x -axis ($1/B$) points. Then, we multiplied the data with a Hanning window function to obtain the periodicity of the experimental data. Finally, we conducted a fast Fourier transform (FFT) on the data. The FFT frequencies F are determined from the peak positions of the FFT spectra obtained by the above procedure. The error bars of the FFT frequencies are defined as the full width at half maximum of the FFT peaks.

DATA AVAILABILITY

The data that support the findings of this study are available from the corresponding author upon reasonable request.

Received: 16 May 2022; Accepted: 16 September 2022;
Published online: 07 October 2022

REFERENCES

- Klitzing, K. V., Dorda, G. & Pepper, M. New method for high-accuracy determination of the fine-structure constant based on quantized hall resistance. *Phys. Rev. Lett.* **45**, 494–497 (1980).
- Tsui, D. C., Stormer, H. L. & Gossard, A. C. Two-dimensional magnetotransport in the extreme quantum limit. *Phys. Rev. Lett.* **48**, 1559–1562 (1982).
- Tsukazaki, A. et al. Quantum hall effect in polar oxide heterostructures. *Science* **315**, 1388–1391 (2007).
- Tsukazaki, A. et al. Observation of the fractional quantum Hall effect in an oxide. *Nat. Mater.* **9**, 889–893 (2010).
- Reyren, N. et al. Superconducting interfaces between insulating oxides. *Science* **317**, 1196–1199 (2007).
- Ando, T., Fowler, A. B. & Stern, F. Electronic properties of two-dimensional systems. *Rev. Mod. Phys.* **54**, 437–672 (1982).
- Mimura, T., Hiyamizu, S., Fujii, T. & Nanbu, K. A new field-effect transistor with selectively doped GaAs/n-Al_xGa_{1-x}As heterojunctions. *Jpn J. Appl. Phys.* **19**, L225–L227 (1980).
- Neupane, M. et al. Observation of a three-dimensional topological Dirac semimetal phase in high-mobility Cd₃As₂. *Nat. Commun.* **5**, 3786 (2014).
- He, L. P. et al. Quantum transport evidence for the three-dimensional dirac semimetal phase in Cd₃As₂. *Phys. Rev. Lett.* **113**, 246402 (2014).
- Moll, P. J. W. et al. Transport evidence for Fermi-arc-mediated chirality transfer in the Dirac semimetal Cd₃As₂. *Nature* **535**, 266–270 (2016).
- Zhang, C. et al. Evolution of Weyl orbit and quantum Hall effect in Dirac semimetal Cd₃As₂. *Nat. Commun.* **8**, 1272 (2017).
- Uchida, M. et al. Quantum Hall states observed in thin films of Dirac semimetal Cd₃As₂. *Nat. Commun.* **8**, 2274 (2017).
- Nishihaya, S. et al. Quantized surface transport in topological Dirac semimetal film. *Nat. Commun.* **10**, 2564 (2019).
- Schumann, T. et al. Observation of the quantum hall effect in confined films of the three-dimensional dirac semimetal Cd₃As₂. *Phys. Rev. Lett.* **120**, 16801 (2018).
- Zhang, C. et al. Quantum Hall effect based on Weyl orbits in Cd₃As₂. *Nature* **565**, 331–336 (2019).
- Xu, S. Y. et al. Discovery of a Weyl fermion semimetal and topological Fermi arcs. *Science* **349**, 613–617 (2015).
- Huang, S. M. et al. A Weyl Fermion semimetal with surface Fermi arcs in the transition metal monopnictide TaAs class. *Nat. Commun.* **6**, 7373 (2015).
- Lv, B. Q. et al. Experimental discovery of weyl semimetal TaAs. *Phys. Rev. X* **5**, 031013 (2015).
- Huang, X. et al. Observation of the chiral-anomaly-induced negative magnetoresistance in 3D weyl semimetal TaAs. *Phys. Rev. X* **5**, 031023 (2015).
- Liu, Z. K. et al. Discovery of a three-dimensional topological dirac semimetal Na₃Bi. *Science* **343**, 864–867 (2014).
- Xiong, J. et al. Evidence for the chiral anomaly in the Dirac semimetal Na₃Bi. *Science* **350**, 413–416 (2015).
- Yang, H. F. et al. Topological Lifshitz transitions and Fermi arc manipulation in Weyl semimetal NbAs. *Nat. Commun.* **10**, 3478 (2019).
- Zhang, C. et al. Ultrahigh conductivity in Weyl semimetal NbAs nanobelts. *Nat. Mater.* **18**, 482–488 (2019).
- Morali, N. et al. Fermi-arc diversity on surface terminations of the magnetic Weyl semimetal Co₃Sn₂S₂. *Science* **365**, 1286–1291 (2019).
- Liu, D. F. et al. Magnetic Weyl semimetal phase in a Kagomé crystal. *Science* **365**, 1282–1285 (2019).
- Belopolski, I. et al. Discovery of topological Weyl fermion lines and drumhead surface states in a room temperature magnet. *Science* **365**, 1278–1281 (2019).
- Takiguchi, K. et al. Quantum transport evidence of Weyl fermions in an epitaxial ferromagnetic oxide. *Nat. Commun.* **11**, 4969 (2020).
- Galletti, L. et al. Two-dimensional Dirac fermions in thin films of Cd₃As₂. *Phys. Rev. B* **97**, 115132 (2018).
- Wang, Z., Weng, H., Wu, Q., Dai, X. & Fang, Z. Three-dimensional dirac semimetal and quantum transport in Cd₃As₂. *Phys. Rev. B* **88**, 125427 (2013).
- Kurebayashi, D. & Nomura, K. Voltage-driven magnetization switching and spin pumping in weyl semimetals. *Phys. Rev. Appl.* **6**, 044013 (2016).
- Araki, Y. & Nomura, K. Charge pumping induced by magnetic texture dynamics in weyl semimetal. *Phys. Rev. Appl.* **10**, 014007 (2018).
- Chen, Y., Bergman, D. L. & Burkov, A. A. Weyl fermions and the anomalous Hall effect in metallic ferromagnets. *Phys. Rev. B* **88**, 125110 (2013).
- Liu, L. et al. Current-induced magnetization switching in all-oxide heterostructures. *Nat. Nanotechnol.* **14**, 939–944 (2019).
- Itoh, S. et al. Weyl fermions and spin dynamics of metallic ferromagnet SrRuO₃. *Nat. Commun.* **7**, 11788 (2016).
- Randall, J. J. & Ward, R. The preparation of some ternary oxides of the platinum metals. *J. Am. Chem. Soc.* **81**, 2629–2631 (1959).
- Wakabayashi, Y. K. et al. Intrinsic physics in magnetic Weyl semimetal SrRuO₃ films addressed by machine-learning-assisted molecular beam epitaxy. *Jpn J. Appl. Phys.* <https://doi.org/10.35848/1347-4065/ac73d8> (2022).
- Wakabayashi, Y. K. et al. Isotropic orbital magnetic moments in magnetically anisotropic SrRuO₃ films. *Phys. Rev. Mater.* **6**, 094402 (2022).
- Wakabayashi, Y. K. et al. Single-domain perpendicular magnetization induced by the coherent $O\ 2p$ -Ru $4d$ hybridized state in an ultra-high-quality SrRuO₃ film. *Phys. Rev. Mater.* **5**, 124403 (2021).
- Eom, C. B. et al. Single-crystal epitaxial thin films of the isotropic metallic oxides Sr_{1-x}Ca_xRuO₃. *Science* **258**, 1766–1769 (1992).
- Izumi, M., Nakazawa, K., Bando, Y., Yoneda, Y. & Terauchi, H. Magnetotransport of SrRuO₃ thin film on SrTiO₃ (001). *J. Phys. Soc. Jpn* **66**, 3893–3900 (1997).
- Koster, G. et al. Structure, physical properties, and applications of SrRuO₃ thin films. *Rev. Mod. Phys.* **84**, 253–298 (2012).
- Shai, D. E. et al. Quasiparticle mass enhancement and temperature dependence of the electronic structure of ferromagnetic SrRuO₃ thin Films. *Phys. Rev. Lett.* **110**, 087004 (2013).
- Takahashi, K. S. et al. Inverse tunnel magnetoresistance in all-perovskite junctions of La_{0.7}Sr_{0.3}MnO₃/SrTiO₃/SrRuO₃. *Phys. Rev. B* **67**, 094413 (2003).
- Li, Z. et al. Reversible manipulation of the magnetic state in SrRuO₃ through electric-field controlled proton evolution. *Nat. Commun.* **11**, 184 (2020).
- Siemons, W. et al. Dependence of the electronics structure of SrRuO₃ and its degree of correlation on cation off-stoichiometry. *Phys. Rev. B* **76**, 075126 (2007).
- Tian, D. et al. Manipulating berry curvature of SrRuO₃ thin films via epitaxial strain. *Proc. Natl Acad. Sci. USA* **118**, e2101946118 (2021).
- Wakabayashi, Y. K. et al. Machine-learning-assisted thin-film growth: Bayesian optimization in molecular beam epitaxy of SrRuO₃ thin films. *APL Mater.* **7**, 101114 (2019).
- Wakabayashi, Y. K. et al. Bayesian optimization with experimental failure for high-throughput materials growth. *Npj Comput. Mater.* **8**, 180 (2022).

49. Snoek, J., Larochelle, H., & Adams, R. P. Paper presented at *Advances in Neural Information Processing Systems 25*. <http://papers.nips.cc/paper/4522-practical-bayesian-optimization> (2012).
50. Wakabayashi, Y. K., Otsuka, T., Taniyasu, Y., Yamamoto, H. & Sawada, H. Improved adaptive sampling method utilizing Gaussian process regression for prediction of spectral peak structures. *Appl. Phys. Express* **11**, 112401 (2018).
51. Mackenzie, A. P. et al. Observation of quantum oscillations in the electrical resistivity of SrRuO₃. *Phys. Rev. B* **58**, R13318 (1998).
52. Wang, Y. et al. Subterahertz momentum drag and violation of matthiessen's rule in an ultraclean ferromagnetic SrRuO₃ metallic thin film. *Phys. Rev. Lett.* **125**, 217401 (2019).
53. Kaneta-Takada, S. et al. Thickness-dependent quantum transport of Weyl fermions in ultra-high-quality SrRuO₃ films. *Appl. Phys. Lett.* **118**, 092408 (2021).
54. Kuroda, K. et al. Evidence for magnetic Weyl fermions in a correlated metal. *Nat. Mater.* **16**, 1090–1095 (2017).
55. Singha, R., Pariari, A. K., Satpati, B. & Mandal, P. Large nonsaturating magnetoresistance and signature of nondegenerate Dirac nodes in ZrSiS. *Proc. Natl Acad. Sci. USA* **114**, 2468–2473 (2017).
56. Xiang, Z. J. et al. Angular-dependent phase factor of shubnikov-de haas oscillations in the dirac semimetal Cd₃As₂. *Phys. Rev. Lett.* **115**, 226401 (2015).
57. Hu, J. et al. π Berry phase and Zeeman splitting of Weyl semimetal TaP. *Sci. Rep.* **6**, 18674 (2016).
58. Abrikosov, A. A. Quantum magnetoresistance. *Phys. Rev. B* **58**, 2788–2794 (1998).
59. Shekhar, C. et al. Extremely large magnetoresistance and ultrahigh mobility in the topological Weyl semimetal candidate NbP. *Nat. Phys.* **11**, 645–649 (2015).
60. Li, Q. et al. Chiral magnetic effect in ZrTe₅. *Nat. Phys.* **12**, 550–554 (2016).
61. Alexander, C. S., McCall, S., Schlottmann, P., Crow, J. E. & Cao, G. Angle-resolved de Haas-van Alphen study of SrRuO₃. *Phys. Rev. B* **72**, 024415 (2005).
62. Nielsen, H. B. & Ninomiya, M. The Adler-Bell-Jackiw anomaly and Weyl fermions in a crystal. *Phys. Lett. B* **130**, 389–396 (1983).
63. Son, D. T. & Spivak, B. Z. Chiral anomaly and classical negative magnetoresistance of Weyl metals. *Phys. Rev. B* **88**, 104412 (2013).
64. Zyuzin, V. A. Magnetotransport of Weyl semimetals due to the chiral anomaly. *Phys. Rev. B* **95**, 245128 (2017).
65. Ramshaw, B. J. et al. Quantum limit transport and destruction of the Weyl nodes in TaAs. *Nat. Commun.* **9**, 2217 (2018).
66. Arnold, F. et al. Negative magnetoresistance without well-defined chirality in the Weyl semimetal TaP. *Nat. Commun.* **7**, 11615 (2016).
67. dos Reis, R. D. et al. On the search for the chiral anomaly in Weyl semimetals: the negative longitudinal magnetoresistance. *N. J. Phys.* **18**, 085006 (2016).
68. Spivak, B. Z. & Andreev, A. V. Magnetotransport phenomena related to the chiral anomaly in Weyl semimetals. *Phys. Rev. B* **93**, 085107 (2016).
69. Lu, H. Z. & Shen, S. Q. Quantum transport in topological semimetals under magnetic fields. *Front. Phys.* **12**, 127201 (2017).
70. Deng, M. X. et al. Quantum oscillation modulated angular dependence of the positive longitudinal magnetoconductivity and planar hall effect in weyl semimetals. *Phys. Rev. B* **99**, 165146 (2019).
71. Yang, Y. Y., Deng, M. X., Duan, H. J., Luo, W. & Wang, R. Q. Electrically tunable kondo effect as a direct measurement of the chiral anomaly in disordered weyl semimetals. *Phys. Rev. B* **101**, 205137 (2020).
72. Liang, S. et al. Experimental tests of the chiral anomaly magnetoresistance in the dirac-weyl semimetals Na₃Bi and GdPtBi. *Phys. Rev. X* **8**, 031002 (2018).
73. Wakabayashi, Y. K., Kaneta-Takada, S., Krockenberger, Y., Taniyasu, Y. & Yamamoto, H. Wide-range epitaxial strain control of electrical and magnetic properties in high-quality SrRuO₃ films. *ACS Appl. Electron. Mater.* **3**, 2712–2719 (2021).
74. Liu, X. et al. Quantum transport of the 2D surface state in a nonsymmorphic semimetal. *Nano Lett.* **21**, 4887–4893 (2021).
75. Lifshitz, I. M. & Kosevich, A. M. Theory of magnetic susceptibility in metals at low temperatures. *Sov. Phys. JETP* **2**, 636–645 (1956).
76. Shoenberg, D. *Magnetic Oscillations in Metals* (Cambridge University Press, 1984).
77. Potter, A. C., Kimchi, I. & Vishwanath, A. Quantum oscillations from surface Fermi arcs in Weyl and Dirac semimetals. *Nat. Commun.* **5**, 5161 (2014).
78. Liang, T. et al. Three-dimensional dirac semimetal and quantum transport in Cd₃As₂. *Nat. Mater.* **14**, 280–284 (2015).
79. Armitage, N. P., Mele, E. J. & Vishwanath, A. Weyl and Dirac semimetals in three-dimensional solids. *Rev. Mod. Phys.* **90**, 015001 (2018).
80. Wang, S., Lin, B. C., Wang, A. Q., Yu, D. P. & Liao, Z. M. Quantum transport in Dirac and Weyl semimetals: a review. *Adv. Phys. X* **2**, 518–544 (2017).
81. Nagaosa, N., Morimoto, T. & Tokura, Y. Transport, magnetic and optical properties of Weyl materials. *Nat. Rev. Mater.* **5**, 621–636 (2020).
82. Hasan, M. Z. et al. Weyl, Dirac and high-fold chiral fermions in topological quantum matter. *Nat. Rev. Mater.* **6**, 784 (2021).
83. Zhang, Y., Bulmash, D., Hosur, P., Potter, A. C. & Vishwanath, A. Quantum oscillations from generic surface Fermi arcs and bulk chiral modes in Weyl semimetals. *Sci. Rep.* **6**, 23741 (2016).
84. Siwakoti, P. et al. Abrupt orthorhombic relaxation in compressively strained ultrathin SrRuO₃ films. *Phys. Rev. Mater.* **5**, 114409 (2021).
85. Roh, C. J. et al. Structural symmetry evolution in surface and interface of SrRuO₃ thin films. *Appl. Surf. Sci.* **553**, 149574 (2021).
86. Cui, Z. et al. Correlation-driven eightfold magnetic anisotropy in a two-dimensional oxide monolayer. *Sci. Adv.* **6**, eaay0114 (2020).
87. Kan, D. et al. Tuning magnetic anisotropy by interfacially engineering the oxygen coordination environment in a transition metal oxide. *Nat. Mater.* **15**, 432–437 (2016).
88. Anwar, M. S. et al. Ferromagnetic SrRuO₃ thin-film deposition on a spin-triplet superconductor Sr₂RuO₄ with a highly conducting interface. *Appl. Phys. Express* **8**, 015502 (2015).
89. Nakai, R. & Nomura, K. Weyl superconductor phases in a Weyl-semimetal/superconductor multilayer. *Phys. Rev. B* **101**, 094510 (2020).
90. Tominaga, J., Kolobov, A. V., Fons, P., Nakano, T. & Murakami, S. Ferroelectric order control of the dirac-semimetal phase in GeTe-Sb₂Te₃ superlattices. *Adv. Mater. Interfaces* **1**, 1300027 (2014).
91. Kar, U. et al. The thickness dependence of quantum oscillations in ferromagnetic Weyl semimetal SrRuO₃. Preprint at <https://doi.org/10.48550/arXiv.2112.13331>(2021).
92. Wakabayashi, Y. K. et al. Structural and transport properties of highly Ru-deficient SrRu_{0.7}O₃ thin films prepared by molecular beam epitaxy: Comparison with stoichiometric SrRuO₃. *AIP Adv.* **11**, 035226 (2021).
93. Nelson, J. B. & Riley, D. R. The thermal expansion of graphite from 15°C. to 800°C.: part I. Experimental. *Proc. Phys. Soc.* **57**, 477–486 (1945).
94. Naito, M. & Sato, H. Stoichiometry control of atomic beam fluxes by precipitated impurity phase detection in growth of (Pr,Ce)₂CuO₄ and (La,Sr)₂CuO₄ films. *Appl. Phys. Lett.* **67**, 2557–2559 (1995).
95. Yamamoto, H., Krockenberger, Y. & Naito, M. Multi-source MBE with high-precision rate control system as a synthesis method sui generis for multi-cation metal oxides. *J. Cryst. Growth* **378**, 184–188 (2013).
96. Wakabayashi, Y. K. et al. Ferromagnetism above 1000 K in a highly cation-ordered double-perovskite insulator Sr₃OsO₆. *Nat. Commun.* **10**, 535 (2019).
97. Imajo, S., Dong, C., Matsuo, A., Kindo, K. & Kohama, Y. High-resolution calorimetry in pulsed magnetic fields. *Rev. Sci. Instrum.* **92**, 043901 (2021).
98. Perdew, J. P., Burke, K. & Ernzerhof, M. Generalized gradient approximation made simple. *Phys. Rev. Lett.* **77**, 3865–3868 (1996).
99. Kresse, G. & Joubert, D. From ultrasoft pseudopotentials to the projector augmented-wave method. *Phys. Rev. B* **59**, 1758–1775 (1999).
100. Kresse, G. & Furthmüller, J. Efficient iterative schemes for ab initio total-energy calculations using a plane-wave basis set. *Phys. Rev. B* **54**, 11169 (1996).
101. Monkhorst, H. J. & Pack, J. D. Special points for Brillouin-zone integrations. *Phys. Rev. B* **13**, 5188–5192 (1976).
102. Liechtenstein, A. I., Anisimov, V. I. & Zaanen, J. Density-functional theory and strong interactions: Orbital ordering in Mott-Hubbard insulators. *Phys. Rev. B* **52**, R5467–R5470 (1995).
103. Mostofi, A. A. et al. An updated version of wannier90: a tool for obtaining maximally-localised Wannier functions. *Phys. Commun.* **185**, 2309–2310 (2014).
104. Martínez, D. G., Souza, I. & Vanderbilt, D. Chiral degeneracies and Fermi-surface Chern numbers in bcc Fe. *Phys. Rev. B* **92**, 085138 (2015).
105. Momma, K. & Izumi, F. VESTA: a three-dimensional visualization system for electronic and structural analysis. *J. Appl. Crystallogr.* **44**, 1272–1276 (2011).

ACKNOWLEDGEMENTS

S.K.T. acknowledges the support from the Japan Society for the Promotion of Science (JSPS) Fellowships for Young Scientists. H.D. acknowledges the support from Grants-in-Aid for Scientific Research No. JP19K05246 and No. JP19H05625 from the Japan Society for the Promotion of Science (JSPS).

AUTHOR CONTRIBUTIONS

Y.K.W. conceived the idea, designed the experiments, and directed and supervised the project. Y.K.W. and Y.Kro. grew the samples. S.K.T. and Y.K.W. carried out the sample characterizations. S.K.T., Y.K.W., and H.I. fabricated the Hall bar structures. S.K.T., Y.K.W., and K.T. carried out the magnetotransport measurements. S.K.T., Y.K.W., T.N., and Y.Koh. performed the high-field magnetotransport measurements. S.K.T. and Y.K.W. analyzed and interpreted the data. S.A.N. and H.D. carried out the electronic-structure calculations. S.K.T. and Y.K.W. co-wrote the paper with input from all authors.

COMPETING INTERESTS

The authors declare no competing interests.

ADDITIONAL INFORMATION

Supplementary information The online version contains supplementary material available at <https://doi.org/10.1038/s41535-022-00511-0>.

Correspondence and requests for materials should be addressed to Yuki K. Wakabayashi.

Reprints and permission information is available at <http://www.nature.com/reprints>

Publisher's note Springer Nature remains neutral with regard to jurisdictional claims in published maps and institutional affiliations.



Open Access This article is licensed under a Creative Commons Attribution 4.0 International License, which permits use, sharing, adaptation, distribution and reproduction in any medium or format, as long as you give appropriate credit to the original author(s) and the source, provide a link to the Creative Commons license, and indicate if changes were made. The images or other third party material in this article are included in the article's Creative Commons license, unless indicated otherwise in a credit line to the material. If material is not included in the article's Creative Commons license and your intended use is not permitted by statutory regulation or exceeds the permitted use, you will need to obtain permission directly from the copyright holder. To view a copy of this license, visit <http://creativecommons.org/licenses/by/4.0/>.

© The Author(s) 2022